RSC Advances

PAPER

View Article Online
View Journal | View Issue

Cite this: *RSC Adv.*, 2018, **8**, 19301

Enhancing the low temperature NH_3-SCR activity of $FeTiO_x$ catalysts *via* Cu doping: a combination of experimental and theoretical study†

Kai Cheng,‡[ab] Weiyu Song,‡[a] Ying Cheng,[a] Huiling Zheng,[a] Lu Wang,[a] Jian Liu,*[a] Zhen Zhao[a] and Yuechang Wei[a]

A series of $Fe_\alpha Cu_{1-\alpha}TiO_x$ catalysts with variable Cu doping amounts was directly synthesized by the sol–gel method and their catalytic performances were tested for the selective catalytic reduction of NO with ammonia. The highest activity was achieved on $Fe_{0.9}Cu_{0.1}Ti$ catalyst. NO conversion was above 80% and N_2 selectivity exceeded 90% on this catalyst in the temperature range of 200–375 °C. High NO and NH_3 oxidation activities facilitated the high NH_3-SCR activities of the catalysts in the low temperature range, while too strong NH_3 oxidation ability resulted in the decline of NH_3-SCR activity. DFT calculations based on the Fe and Cu co-doping TiO_2 model showed that the barrier of NH_3 activation is dramatically reduced as compared to pure Fe doping. This is due to the lowered p-band of lattice O. However, such activated O will also strongly decrease the barrier for the dissociation of NH_2 to NH species, which will lead to the formation of N_2O. Both Brønsted and Lewis acid sites over $Fe_{0.9}Cu_{0.1}Ti$ catalyst are involved in the NH_3-SCR reaction. The adsorption of NO_x is strong in the low temperature range, and large amounts of nitrates were decomposed on the catalyst surface in the high temperature range.

Received 5th April 2018
Accepted 13th May 2018

DOI: 10.1039/c8ra02931h

rsc.li/rsc-advances

1. Introduction

Fast urbanization and the rapid development of industry have caused serious air pollution and stringent regulations are being released with growing environmental awareness. It is generally considered that air pollution is predominantly from the combustion processes of fossil fuels in power plants, vehicles and other incineration processes. Among various air contaminants, nitrogen oxides (NO_x) are notable and are known as the major causes of photochemical smog, haze, acid rain, ozone depletion and the greenhouse effect. Selective catalytic reduction of NO_x with NH_3 (NH_3-SCR) is a powerful technique for the abatement of NO_x from stationary sources. WO_3 (MoO_3) modified V_2O_5/TiO_2 are the current commercially used catalysts for NH_3-SCR in industry. However, some disadvantages still exist in these catalyst systems, including high working temperature, toxicity of vanadium species and low N_2 selectivity at high temperatures. Therefore, many researchers are trying to develop new NH_3-SCR catalysts with high deNO_x efficiency, high N_2 selectivity, excellent hydrothermal stability and insensitivity to co-existing poisoning components in the SCR atmosphere, such as H_2O, SO_2 or alkali metals.[1–3]

Recently, Fe-based catalysts have attracted much attention for the SCR reaction.[4–6] For example, $FeTiO_x$ catalyst is more active than crystalline Fe_2O_3 and TiO_2. The active iron titanate crystallites in $FeTiO_x$ catalyst prepared at low calcination temperature were mainly in the form of a specific edge-shared Fe^{3+}–$(O)_2$–Ti^{4+} structure. However, the catalytic activity of $FeTiO_x$ catalyst is low at low temperature.[7–10] It is essential to enhance the low-temperature SCR activity of $FeTiO_x$ catalyst. Among the alternatives of active components examined for the low-temperature SCR reaction, copper has been widely explored owing to its efficacy and relatively low cost.[11–14] It is well known that the SCR performance of catalysts depends on the dispersion, nuclearity and oxidation state of the active components, which could be efficiently controlled by the preparation method.[15,16]

In the present work, a series of $Fe_\alpha Cu_{1-\alpha}TiO_x$ catalysts with variable Cu doping amounts was directly synthesized by the sol–gel method and applied in the NH_3-SCR process. The obtained $Fe_{0.9}Cu_{0.1}TiO_x$ catalysts exhibited excellent SCR activity. Based on this result, the effects of Cu substitution amounts on the structure, acidity and redox properties of the $Fe_\alpha Cu_{1-\alpha}TiO_x$ catalysts were also studied. The reactivity of surface-adsorbed NH_3 and NO_x species on the $Fe_{0.9}Cu_{0.1}TiO_x$ catalysts was investigated using *in situ* diffused reflectance infrared Fourier transformed spectroscopy (DRIFTS) technique.

[a]*State Key Laboratory of Heavy Oil Processing, China University of Petroleum, 18# Fuxue Road, Chang Ping District, Beijing, 102249, China. E-mail: liujian@cup.edu.cn; Fax: +86-10-69724721; Tel: +86-10-89732326*

[b]*Department of Mechanical and Automation Engineering, The Chinese University of Hong Kong, New Territories, Hong Kong SAR, Shatin, China*

† Electronic supplementary information (ESI) available. See DOI: 10.1039/c8ra02931h

‡ The two authors contribute equally to this work.

2. Experimental and computational details

2.1. Catalyst preparation

$Fe_\alpha Cu_{1-\alpha}TiO_x$ catalysts were prepared by the sol–gel method. All chemicals used were of analytical grade. A solution of 34 ml of butyl titanate (Sinopharm Chemical Reagent Co., Ltd, ≥98.0%) and 136 ml of anhydrous ethanol (Sinopharm Chemical Reagent Co., Ltd, ≥99.7%) was added dropwise to another solution of 34 ml of deionized water, 34 ml of anhydrous ethanol, 6.8 ml of nitric acid (Sinopharm Chemical Reagent Co., Ltd, 65.0–68.0%) and a certain amount of ferric nitrate (Sinopharm Chemical Reagent Co., Ltd, ≥98.0%) and copper nitrate (Sinopharm Chemical Reagent Co., Ltd, ≥98.0%) at room temperature under vigorous stirring to carry out hydrolysis. After continuously stirring for 3 h, the yellowish transparent sol was yielded. Subsequently, the sol was dried at 80 °C for 24 h to form a xerogel. After being crushed and sieved through a 60–100 mesh, the xerogel was calcinated at 500 °C for 5 h in air. The catalysts were denoted as $Fe_\alpha Cu_{1-\alpha}TiO_x$, where α represents the molar ratio of n(Fe)/n(Fe + Cu).

2.2. Physical and chemical characterization

The crystal structures of the fresh catalysts were determined with a powder X-ray diffractometer using Cu Kα ($\lambda = 0.1542$ nm) radiation combined with a nickel filter operating at 40 kV and 10 Ma (Shimadzu, Japan). The diffractometer data were recorded for 2θ values from 10° to 80° at a scanning rate of 4° min^{-1}. The patterns were compared with ICDD files for phase identification.

The Brunauer–Emmett–Teller (BET) surface areas were measured by N_2 adsorption and desorption (Quantachrome Instruments, USA). The samples were degassed at 200 °C for 12 h.

TEM images were obtained using a JEOL JEM 2100 electron microscope equipped with a field emission source at an accelerating voltage of 200 kV. Drops of the suspension were applied and, after drying, the fine particles were well dispersed on a copper grid coated with carbon. The elemental local mapping was acquired by energy-dispersive spectroscopy (EDS) using a Tecnai F20 electron microscope equipped with a STEM unit and a CCD detector.

X-ray photoelectron spectroscopy (XPS) spectra were recorded with a standard AlK source (1486.6 eV) working at 350 W (XSAM800, Kratos Analytical Ltd, UK). The working pressure was less than 2×10^{-7} Pa. The spectrometer was calibrated by assuming the binding energy (BE) of the Au $4f_{7/2}$ line to lie at 84.0 eV with respect to the Fermi energy level. The binding energies of Ce 3d and O 1s were calibrated using the C 1s peak (BE = 284.8 eV) as the standard.

Temperature-programmed reduction with H_2 (H_2-TPR) experiments were performed using a Quantachrome Instruments Autosorb IQ. A 100 mg sample was pretreated under Ar by calcination at 300 °C for 1 h and subsequently cooled to 30 °C. Afterwards, 10% H_2/Ar flow (60 ml min^{-1}) was passed over the catalyst bed while the temperature was ramped from 30 to 800 °C at a heating rate of 10 °C min^{-1}.

The nature of the acid sites of the catalysts was determined by pyridine-IR (Py-IR) on a Magna IR 560 FT-IR instrument with a resolution of 4 cm^{-1}. The samples were dehydrated at 500 °C for 5 h under a vacuum of 1.33×10^{-3} Pa, followed by the adsorption of purified pyridine vapor at room temperature for 20 min. The system was then degassed and evacuated at different temperatures, and Py-IR spectra were recorded.

In situ DRIFTS spectra were recorded using a thermo Nicolet IS50 spectrometer, which was equipped with a high-temperature environmental cell fitted with a ZnSe window and an MCT detector cooled with liquid N_2. The catalyst was loaded in the Harrick IR cell and heated to 400 °C under N_2 at a total flow rate of 50 ml min^{-1} for 60 min to remove adsorbed impurities. A background spectrum was collected under a flowing N_2 atmosphere and was subtracted from the sample spectra. The DRIFTS spectra were recorded by accumulating 32 scans with a resolution of 4 cm^{-1}.

2.3. Activity measurements

The activity tests of the various catalysts for the NH_3-SCR of NO were carried out in a fixed bed quartz reactor (i.d. 6 mm). The feed gas mixture consisted of 1000 ppm of NO, 1000 ppm of NH_3, 3 vol% of O_2 and Ar-balanced gas. A total flow rate of 500 ml min^{-1} was maintained for all experiments. The concentrations of NO in the inlet and outlet gas were measured by a flue gas analyzer (Model-4000VM, SIGNAL International Ltd., UK). Meanwhile, the concentrations of NH_3, NO, NO_2 and N_2O were measured by an FTIR spectrometer (Nicolet IS50). All catalysts were kept on stream at each temperature for 30 min. NO conversion was defined as follows:

$$\text{NO conversion}(\%) = \frac{NO_{(inlet)} - NO_{(outlet)}}{NO_{(inlet)}} \times 100\% \quad (1)$$

where $NO_{(inlet)}$ represents the NO concentration in the inlet (ppm) and $NO_{(outlet)}$ represents the NO concentration in the outlet (ppm).

N_2 selectivity in the SCR reaction was calculated from eqn (2).

$$N_2 \text{ selectivity}(\%) = \frac{2[N_2]_{out}}{2[N_2]_{out} + 2[N_2O]_{out} + [NO_2]_{out}} \times 100\% \quad (2)$$

2.4. Computational details

In this work, the Vienna ab initio simulation package (VASP)[17,18] was used to calculate all states with the electron exchange correlation effect described by the Perdew–Burke–Ernzerhof functional within the generalized gradient approximation (GGA-PBE).[19] The calculations involved on-site Coulomb corrections[20] (DFT+U, $U_{eff} = 4.2$ eV for Ti 3d states, 6.0 eV for Cu 3d state, 4.5 eV for Mn 3d states). The spin-polarized calculations were performed. PAW pseudopotential was used to describe the core–valence electron interaction.[21] A plane-wave basis set with an energy cutoff of 400 eV was used in this

work. The climbing nudged elastic band method (CI-NEB)[22,23] was employed to locate the transition states. The anatase TiO_2 (101) surface was presented by a six-layer slab model with a vacuum gap of 15 Å. For all the surface calculations, the model was a periodic slab with a (2×2) surface unit cell. A Monkhorst pack $2 \times 2 \times 1$ k-point mesh was used for the Brillouin zone integration. During structural optimizations, all of the atoms except those in the bottom two TiO_2 layers of the slab were allowed to relax until atom forces were smaller than 0.05 eV $Å^{-1}$. Adsorption energy was calculated using the following expression: $E_{ad} = E_{tot} - E_{slab} - E_x$. E_{tot} is the total energy of the combined system with the adsorbate X bound to the slab, E_{slab} is the energy of the slab alone, and E_x is the energy of the adsorbate in the gas phase. According to this definition, exothermic adsorption results in a negative value of E_{ad}.

3. Results and discussion

3.1. SCR performance

Fig. 1 shows the NH_3-SCR performance as a function of temperature on the $Fe_\alpha Cu_{1-\alpha}TiO_x$ catalysts with GHSV = 50 000 h^{-1}. The $FeTiO_x$ catalyst showed very narrow operation temperature windows, and 80% NO conversion was obtained at a higher temperature of 275 °C. The temperature at which NO conversion exceeded 80% decreased to 255 °C for $Fe_{0.95}Cu_{0.05}$-TiO_x and about 150 °C for $CuTiO_x$. The temperature range for optimum NO reduction (>80%) extends toward lower temperatures. Thus, copper oxide plays an important role in the low-temperature NH_3-SCR reaction.[16] Among these catalysts, the $Fe_{0.9}Cu_{0.1}TiO_x$ catalyst with the molar ratio of Fe : Cu = 9 : 1 showed the best activity with NO conversion above 80% from 200 °C to 375 °C. Comparatively, the maximal NO conversion on $CuTiO_x$ only reached 89%, indicating that CuO_x addition can remarkably enhance the low-temperature NH_3-SCR activity of $FeTiO_x$ catalysts and broaden the temperature window for NO conversion.

Fig. 1b shows the NH_3 conversion as a function of temperature over various catalysts during the NH_3-SCR reaction. The NH_3 conversion monotonously increased with increasing of the Cu doping amount in the $Fe_\alpha Cu_{1-\alpha}TiO_x$ catalysts. At a temperature of 150 °C the $CuTiO_x$ catalysts gave an ammonia conversion above 80% and this was maintained above 90% in the temperature range of 200–400 °C. The results indicate that gaseous NH_3 is activated more easily on Cu-containing catalysts, thus the Cu-containing catalysts showed better low-temperature activity than $FeTiO_x$ catalysts.

DFT calculations were then performed to gain a better understanding of the role of doping Cu in enhancing the reactivity. As shown in Fig. S1,† NH_3 adsorbs on the Cu–Fe–TiO_2 surface with an adsorption energy of −0.92 eV, 0.08 eV stronger than that on the Fe–TiO_2 surface. This suggests that Cu doping can slightly enhance NH_3 adsorption. As shown in previous studies, the dissociation of adsorbing NH_3 is the rate-limiting step of the NH_3-SCR reaction.[24–26] The activation barrier of this step was calculated on the two comparative models (Fe–Cu–TiO_2 and Fe–TiO_2). The H of adsorbed NH_3 can be dissociated to surface O atom to form NH_2 species with an energy barrier of

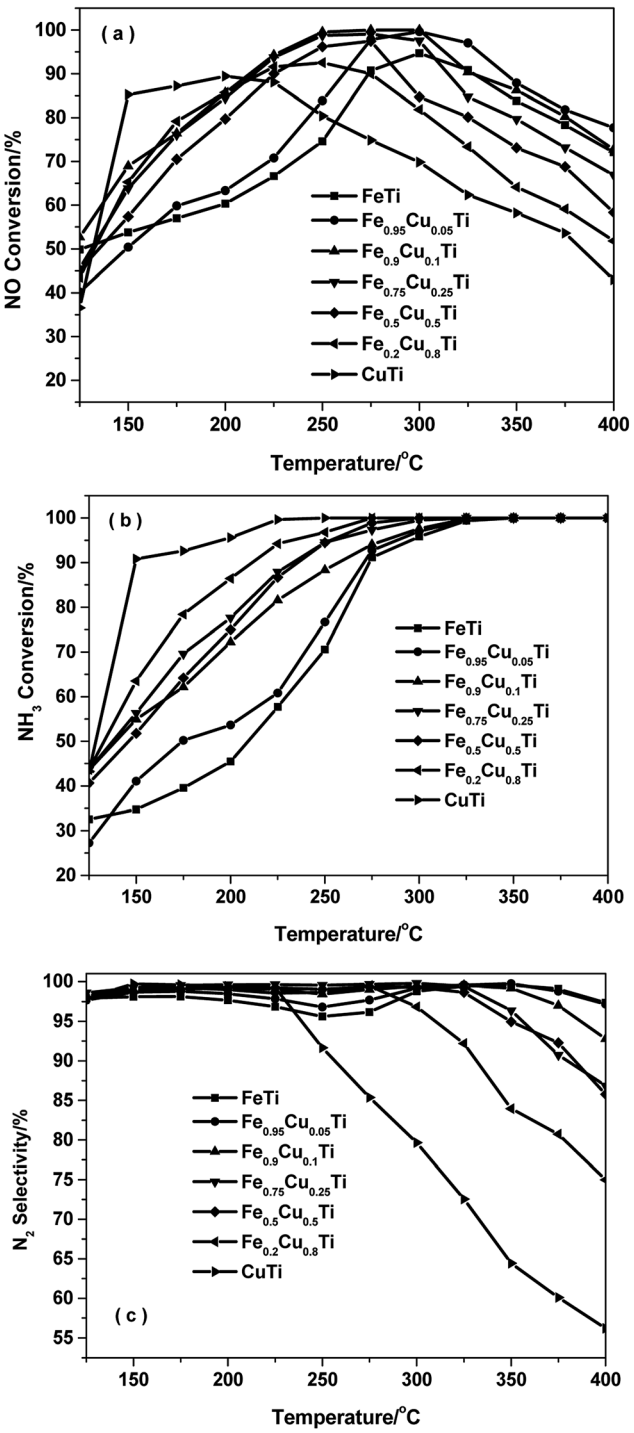

Fig. 1 NH_3-SCR performance as a function of temperature on Fe_α-$Cu_{1-\alpha}TiO_x$ catalysts with GHSV = 50 000 h^{-1}. (a) NO conversion, (b) NH_3 conversion and (c) N_2 selectivity.

0.64 eV, which is 0.71 eV lower than that on Fe–TiO_2. The lower energy barrier of NH_3 dissociation indicates higher SCR activity, consistent with the experimental results. The calculated density of states (DOS) (Fig. 2a) shows that the energy level of the conduction band of the active O p on Cu–Fe–TiO_2 is lower than that on Fe–TiO_2. This is owing to the strong interaction between

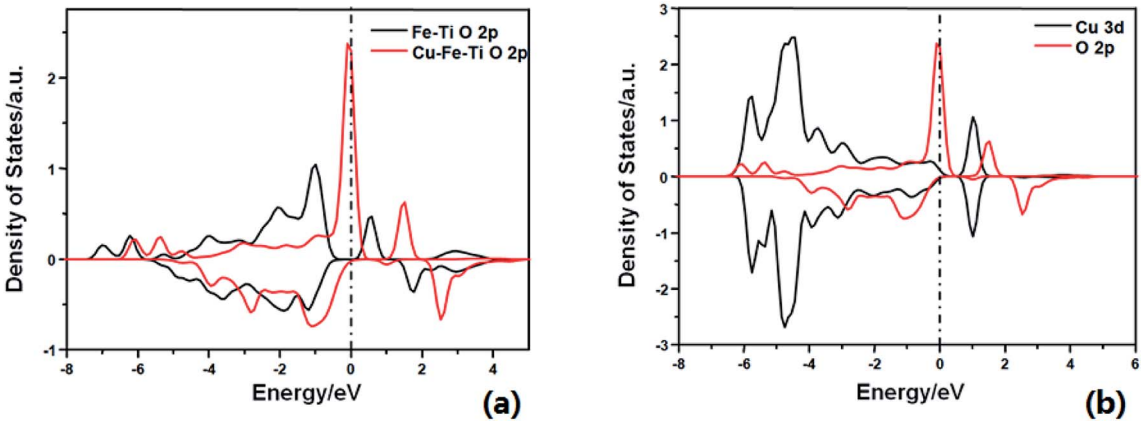

Fig. 2 Calculated projected density of states for (a) O 2p on Fe–TiO_2 surface (black) and Cu–Fe–TiO_2 surface (red); (b) Cu 3d (black) and O 2p (red) on Cu–Fe–TiO_2 surface.

Cu d bands and the O p band, which strongly changed the electron state of the neighboring O atom (Fig. 2b). From the electronic point of view, the essence of NH_3 dissociation with one H to the lattice O involves one electron being added to the conduction band of the O p orbital. The lower the conduction band, the easier the process. This explains the calculated lower energy barrier.

Fig. 1c shows the N_2 selectivity for the NH_3-SCR of NO over $Fe_\alpha Cu_{1-\alpha}TiO_x$ catalysts. Although the substitution of Fe by Cu in iron titanate catalyst could enhance the low-temperature SCR activity, the N_2 selectivity had an obvious decrease owing to the production of N_2O with the increasing of the Cu molar amount, especially at high temperatures above 250 °C. The further dissociation of NH_2 to NH will lead to the formation of N_2O. The calculated energy barrier is 0.76 eV for this step on Fe–Cu– TiO_2, which is 0.38 eV lower than NH_2 dissociation on Fe–TiO_2. This explains the experimental result that the N_2 selectivity had an obvious decrease owing to the production of N_2O on the Cu–Fe–TiO_2 catalyst.

3.2. NH_3 and NO oxidation activities of $Fe_\alpha Cu_{1-\alpha}TiO_x$ catalysts

A previous study[13] showed that the N_2 selectivity in the SCR reaction had a strong inverse correlation with the oxidation of NH_3, therefore separate NH_3 oxidation experiments were also conducted over $Fe_\alpha Cu_{1-\alpha}TiO_x$ catalysts. As shown in Fig. 3, the NH_3 conversions had an obvious enhancement with the increasing of Cu substitution amounts, and the highest NH_3 conversions were obtained over the $CuTiO_x$ catalyst. However, the N_2 selectivity showed an obvious decrease in NH_3 oxidation reactions at the same time, which is in accordance with the changing trend of N_2 selectivity in the SCR reaction. This implies that although the NO oxidation activity is enhanced when Fe is partially substituted by Cu, which is beneficial to the promotion of SCR activity, the unselective oxidation of NH_3 to N_2O, NO or NO_2 in the SCR conditions is also enhanced, resulting in the production of a large amount of by-products. There should be a compromise between the SCR activity and N_2 selectivity when we determine on the Cu substitution amount in practical applications.

It was reported that the enhancement of NO oxidation to NO_2 over SCR catalysts could significantly promote the low-temperature activity owing to the occurrence of "fast SCR": $4NH_3 + 2NO + 2NO_2 + O_2 \rightarrow 4N_2 + 6H_2O$.[27–29] The effect of NO_2 and the detailed "fast SCR" reaction mechanism have been studied extensively over conventional V_2O_5–WO_3/TiO_2 and Fe–zeolite catalysts (such as Fe/HBEA and Fe/ZSM-5) by many researchers. In this study, the effect of Cu substitution amounts on the NO oxidation activity of iron titanate catalysts was also investigated and the results are shown in Fig. 4. With the increasing of Cu substitution amounts, the NO conversion to NO_2 showed an obvious enhancement, and the maximum conversions were obtained over $CuTiO_x$ catalyst. Although the NO oxidation activity of $CuTiO_x$ was higher than that of $Fe_{0.9}Cu_{0.1}TiO_x$, the SCR activity over the former catalyst was still much lower than that over the latter one, as shown in Fig. 4.

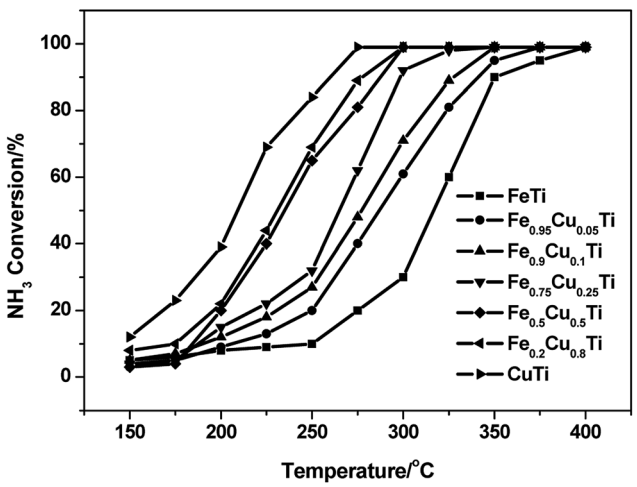

Fig. 3 NH_3 oxidation profile of $Fe_\alpha Cu_{1-\alpha}TiO_x$ catalysts. Reaction conditions: $[NH_3]$ = 1000 ppm, $[O_2]$ = 3%, balance N_2 and GHSV = 50 000 h^{-1}.

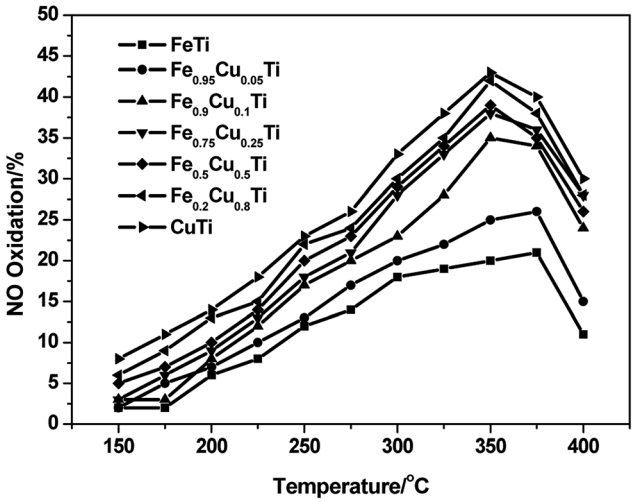

Fig. 4 NO oxidation profile of $Fe_\alpha Cu_{1-\alpha}TiO_x$ catalysts. Reaction conditions: [NO] = 1000 ppm, [O_2] = 3%, balance N_2 and GHSV = 50 000 h^{-1}.

This implies that the SCR activity over $CuTiO_x$ catalyst is not just related to the NO oxidation activity.

3.3. XRD results

Powder XRD patterns of $Fe_\alpha Cu_{1-\alpha}TiO_x$ catalysts are shown in Fig. 5. $FeTiO_x$ catalyst showed no obvious sharp diffraction peaks besides some broad bumps, implying that this catalyst was mainly in the form of amorphous iron titanate, which were thought to be the real active phases. With the increasing of Cu molar amount from 0 to 0.25, XRD patterns of $Fe_\alpha Cu_{1-\alpha}TiO_x$ catalysts exhibited no significant variation, indicating that these samples were still in an amorphous state. The part substitution of Fe by Cu did not destroy the catalyst structures. However, when Cu substitution amounts increased to above 0.25, TiO_2 and CuO phase peak appeared, which indicated that the amorphous state structure was destroyed. The negligible effect of increasing Cu amount above 0.25 on the SCR activity is related to this change.

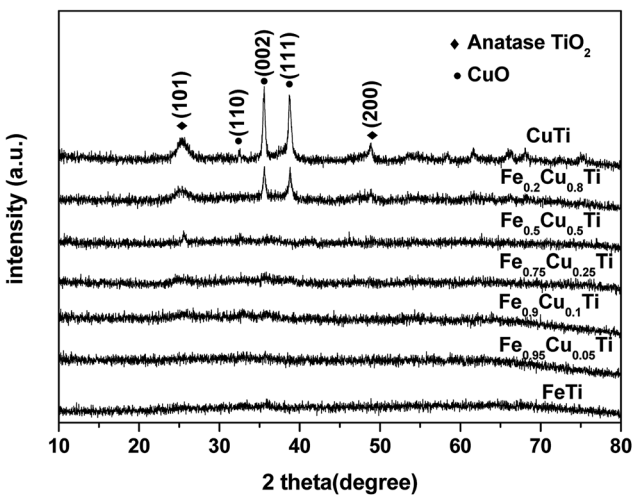

Fig. 5 X-ray diffraction patterns of $Fe_\alpha Cu_{1-\alpha}TiO_x$.

3.4. BET results

Fig. S2† shows the nitrogen adsorption–desorption isotherms and the corresponding pore size distribution curves of the $Fe_\alpha Cu_{1-\alpha}TiO_x$ catalysts. The isotherms for the $Fe_\alpha Cu_{1-\alpha}TiO_x$ catalysts are similar to typical type IV isotherms, which are characteristic of mesoporous materials. In the diameter range below 3 nm, the adsorbed volume on the $Fe_{0.9}Cu_{0.1}TiO_x$ catalyst was highest among all catalysts. This means that the $Fe_{0.9}Cu_{0.1}Ti$ sample included the most abundant micropores or mesopores, which can supply a greater inner surface area for the occurrence of the SCR reaction. The BET surface areas in Table 1 also followed such a sequence, which is in good agreement with the sequence of SCR activity. The $Fe_{0.9}Cu_{0.1}Ti$ catalyst exhibited the largest BET surface area, which is beneficial to the NH_3-SCR process.

3.5. TEM results

Fig. 6 shows the TEM/HRTEM images of the $Fe_{0.9}Cu_{0.1}Ti$ and $Fe_{0.5}Cu_{0.5}Ti$ catalysts. Both catalysts were made of nanoparticles in the size range of 15–30 nm, as shown in Fig. 6a and c. For the $Fe_{0.9}Cu_{0.1}Ti$ catalyst, no interplanar distances of Fe_2O_3, CuO and TiO_2 were seen on the surface of the catalyst. This suggests the formation of the homogeneous phase of Fe_2O_3, CuO and TiO_2, which is consistent with the XRD results. For the $Fe_{0.5}Cu_{0.5}Ti$ catalyst, two phases with the interplanar spacing are shown in Fig. 6d, corresponding to the interplanar distances of CuO and TiO_2 planes, respectively. The results mean that the amorphous state structure was destroyed on the $Fe_{0.5}Cu_{0.5}Ti$ catalyst.

3.6. Py-IR results

FTIR spectroscopy of adsorbed pyridine was performed to study the acid properties of the $FeTiO_x$ and $Fe_{0.9}Cu_{0.1}TiO_x$ samples. As shown in Fig. 7, the bands located at 1540 and 1640 cm^{-1} are assigned to pyridinium ions adsorbed on Brønsted sites. The bands located at 1440, 1455 and 1630 cm^{-1} are due to pyridinium ions adsorbed on Lewis sites. Brønsted and Lewis acid sites were observed in both $FeTiO_x$ and $Fe_{0.9}Cu_{0.1}TiO_x$ catalysts, where Lewis acid sites prevail over Brønsted acid sites at 200 °C.

Table 1 The textural and structural properties of all catalysts

Samples	S_{BET} ($m^2\ g^{-1}$)	V_{mic} ($cm^2\ g^{-1}$)	Average pore diameter (nm)
$FeTiO_x$	185.2	0.30	4.6
$Fe_{0.95}Cu_{0.05}TiO_x$	187.0	0.27	4.3
$Fe_{0.9}Cu_{0.1}TiO_x$	244.5	0.27	5.1
$Fe_{0.75}Cu_{0.25}TiO_x$	121.2	0.23	5.1
$Fe_{0.5}Cu_{0.5}TiO_x$	128.1	0.23	4.8
$Fe_{0.2}Cu_{0.8}TiO_x$	104.7	0.21	5.2
$CuTiO_x$	89.1	0.20	5.9

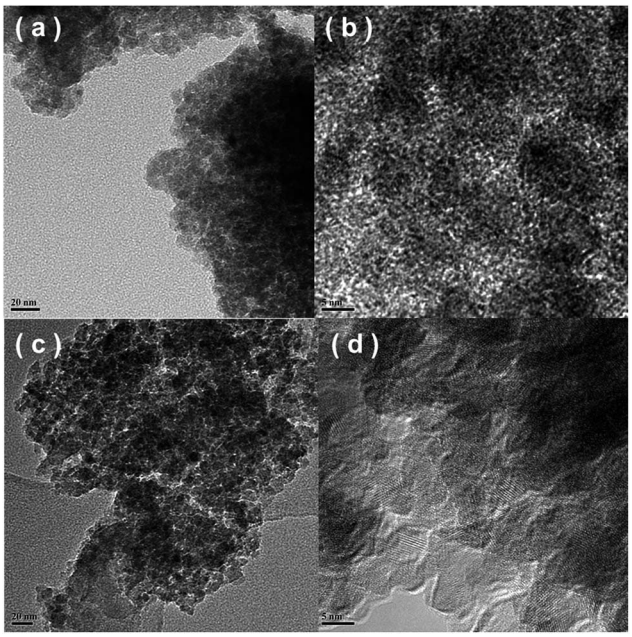

Fig. 6 TEM/HRTEM images of $Fe_{0.9}Cu_{0.1}TiO_x$ (a and b) and $Fe_{0.5}Cu_{0.5}TiO_x$ (c and d).

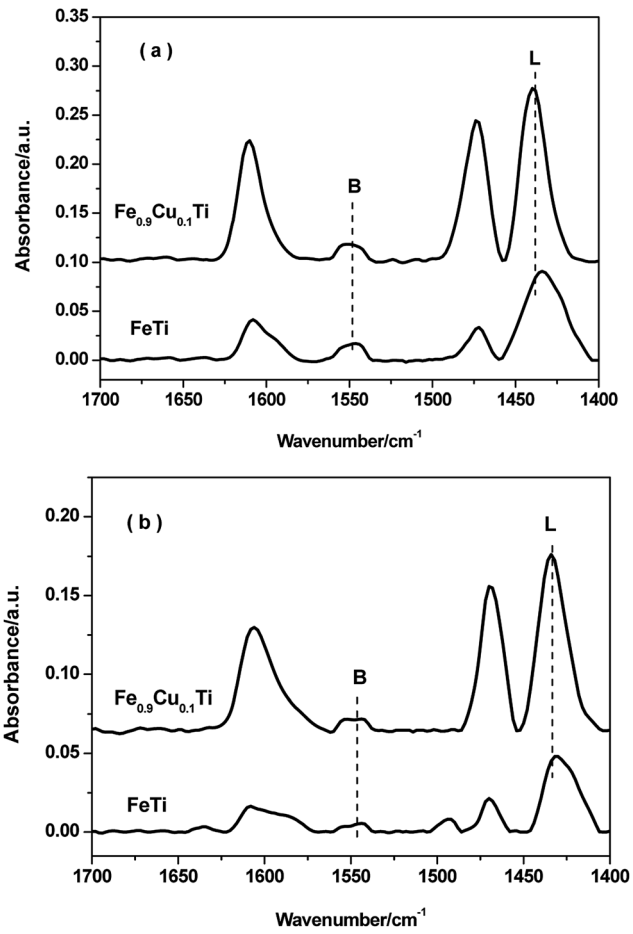

Fig. 7 FT-IR spectra of pyridine adsorbed on $FeTiO_x$ and $Fe_{0.9}Cu_{0.1}TiO_x$ after degassing at 200 °C and 350 °C.

When the adsorption temperature was increased to 350 °C, the intensities of the Lewis and Brønsted peaks decreased. It can be seen that Lewis and Brønsted acid sites are more abundant in the $Fe_{0.9}Cu_{0.1}TiO_x$ catalyst than in the $FeTiO_x$ catalyst. The more Lewis acid sites over the $Fe_{0.9}Cu_{0.1}TiO_x$ catalyst would not be attributed to the addition of Cu substance with abundant Lewis acid sites, but the changes in catalyst structure and electron charge density caused by the generation of Ti–O–Fe mixed bonds. It has been reported that the acid sites may interact with the active components, and therefore inhibit the agglomeration of the active components. Moreover, the increasing of Lewis acid sites would promote the SCR performance by enhancing the activation of NH_3.

3.7. XPS results

Fig. 8a shows the XPS results for Fe 2p. Two characteristic peaks ascribed to Fe $2p_{3/2}$ at 710.1 eV and Fe $2p_{1/2}$ at 723.7 eV appeared for each Fe-containing sample, indicating that the iron species in these samples are in the Fe^{3+} oxidation state. With the increasing of Cu substitution amounts, the intensities of the Fe $2p_{3/2}$ and Fe $2p_{1/2}$ peaks gradually decreased owing to the concentration reduction of surface iron species. However, the corresponding binding energies do not show variation, implying that the differences in the SCR over these catalysts are not caused by the redox ability after changing the iron species state.

Fig. 8b shows the XPS spectra of Ti 2p in all catalysts. Two characteristic peaks at *ca.* 457.3 and 463.1 eV appear with the increasing of the Cu molar content from 0 to 0.5, which are assigned to Ti $2p_{3/2}$ and Ti $2p_{1/2}$. On further increasing the Cu doping amount, the binding energies of Ti $2p_{3/2}$ and Ti $2p_{1/2}$ in relevant samples are shifted toward higher BE by 0.5 eV. Combined with the XRD results, this phenomenon may be due to the phase transformation.

Fig. 8c shows XPS spectra of Cu 2p in all catalysts. The Cu $2p_{3/2}$ signal is composed of two peaks at 933.6 eV and 934.5 eV, where the former is assigned to the presence of CuO species[30,31] and the latter to Cu^{2+} species. Cu^{2+} species are detected when the Cu doping amount is below 0.25. Further increasing the Cu doping amount to above 0.25, the catalysts are in the CuO phase. It indicates that the Cu^{2+} species transform to the CuO phase when the Cu substitution amount increases to above 0.25. This result is also consistent with the XRD results. CuO could accelerate NH_3 oxidation and, as a result, the transformation of Cu species from Cu^{2+} to CuO would cause the decrease of the selectivity of the $Fe_\alpha Cu_{1-\alpha}TiO_x$ catalysts.

3.8. *In situ* DRIFTS studies

3.8.1. Adsorption of NH_3. Fig. 9 shows the *in situ* DRIFT spectra of NH_3 adsorption over $FeTiO_x$ and $Fe_{0.9}Cu_{0.1}TiO_x$ catalysts at different temperatures. When NH_3 was introduced into the DRIFTS cell at room temperature, several vibration bands could be detected in the range of 1000–4000 cm^{-1}. For the $FeTiO_x$ catalyst (Fig. 9a), the bands at 1602 and 1209 cm^{-1} can be assigned to the asymmetric and symmetric bending vibrations of the NH bond in the NH_3 coordinately linked to the

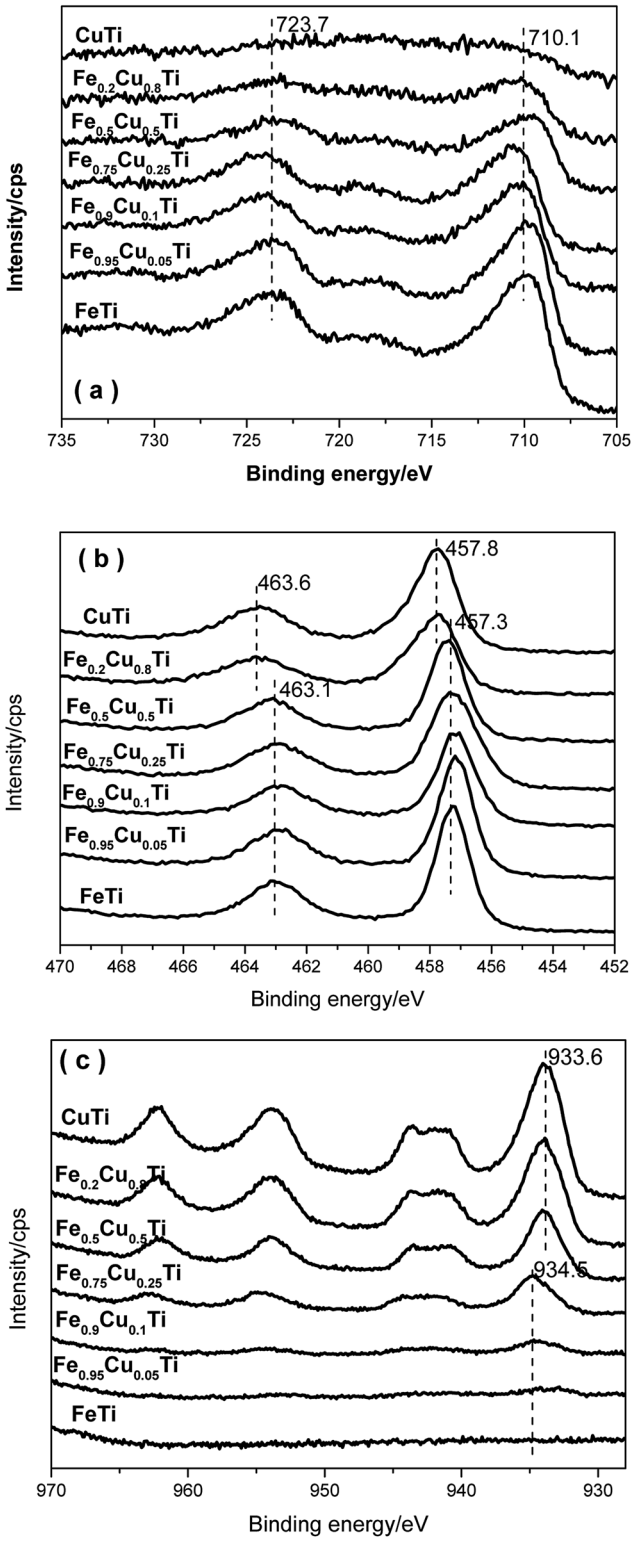

Fig. 8 XPS spectra of (a) Fe 2p, (b) Ti 2p and (c) Cu 2p in $Fe_{\alpha}Cu_{1-\alpha}TiO_x$ catalysts.

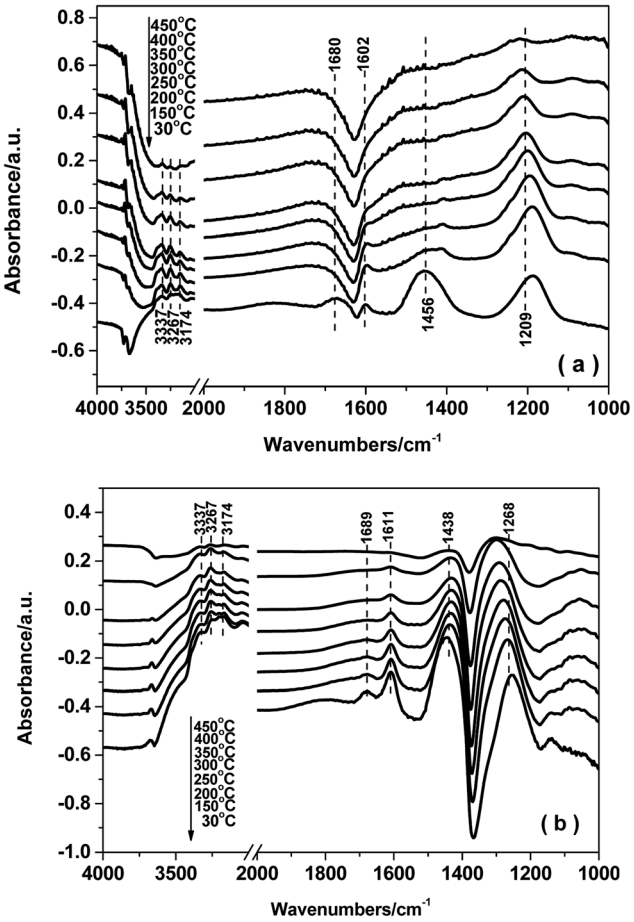

Fig. 9 *In situ* DRIFTS of NH_3 desorption on $FeTiO_x$ (a) and $Fe_{0.9}Cu_{0.1}TiO_x$ (b).

Lewis acid site, respectively. The peaks at 3337, 3267 and 3174 cm^{-1} can be ascribed to the N–H stretching vibration modes of the coordinated NH_3, while the band at 1456 cm^{-1} is due to the asymmetric bending vibration of NH bond in NH^{4+} chemisorbed on the Brønsted acid site.[32,33] These adsorbed NH_3 species decreased with the increasing of the temperature and the band attributed to the Brønsted acid site disappears at 200 °C. Fig. 9b shows the *in situ* DRIFT spectra of NH_3 adsorption over the $Fe_{0.9}Cu_{0.1}TiO_x$ catalyst. Both the intensities of the Lewis acid site and Brønsted acid sites on $Fe_{0.9}Cu_{0.1}TiO_x$ catalyst are higher than those on $FeTiO_x$ catalyst. It is also noticeable that the band attributed to the Brønsted acid site does not disappear completely even at 450 °C. The obtained results suggested that there are more abundant acid sites and the Brønsted acid sites are more stable with the introduction of Cu. Previous reports showed that Brønsted acid sites were beneficial to the adsorption of NH_3, thus improving the low-temperature activity.

3.8.2. Co-adsorption of NO and O_2. Fig. 10a shows the *in situ* DRIFT spectra of NO + O_2 desorption on the $FeTiO_x$ catalyst at different temperatures. The peaks at 1605, 1579, 1294 and 1254 cm^{-1} were attributed to the asymmetric frequencies of bridged nitrate (1605 and 1254 cm^{-1}), bidentate nitrate (1579 cm^{-1}), and monodentate nitrate (1294 cm^{-1}) at room temperature. With the introduction of Cu, a new peak at 1897 cm^{-1} at room temperature appeared in Fig. 10b, which was assigned to the asymmetric frequency of Cu^{2+}–NO.[34,35]

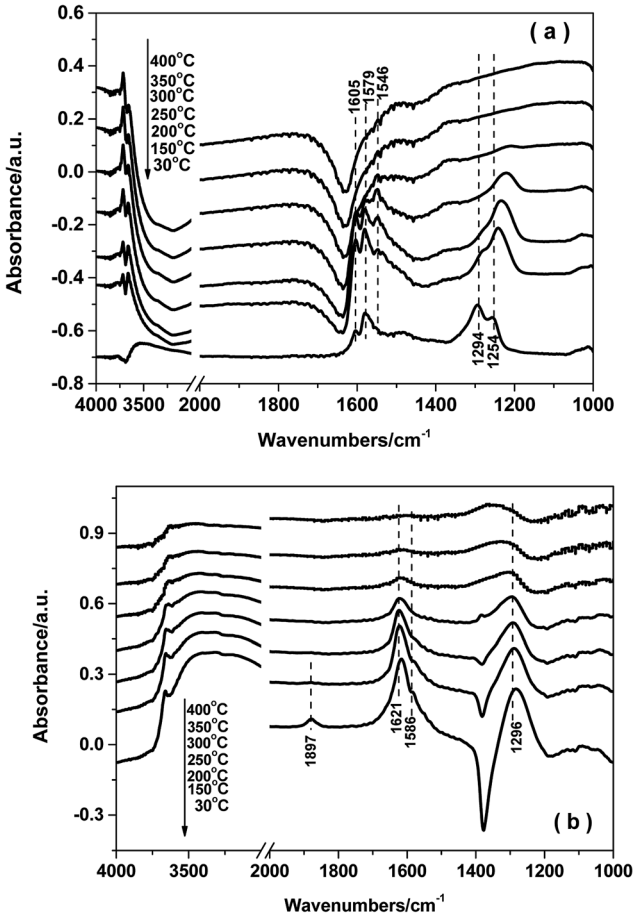

Fig. 10 *In situ* DRIFTS of NO + O_2 desorption on $FeTiO_x$ (a) and $Fe_{0.9}Cu_{0.1}TiO_x$ (b).

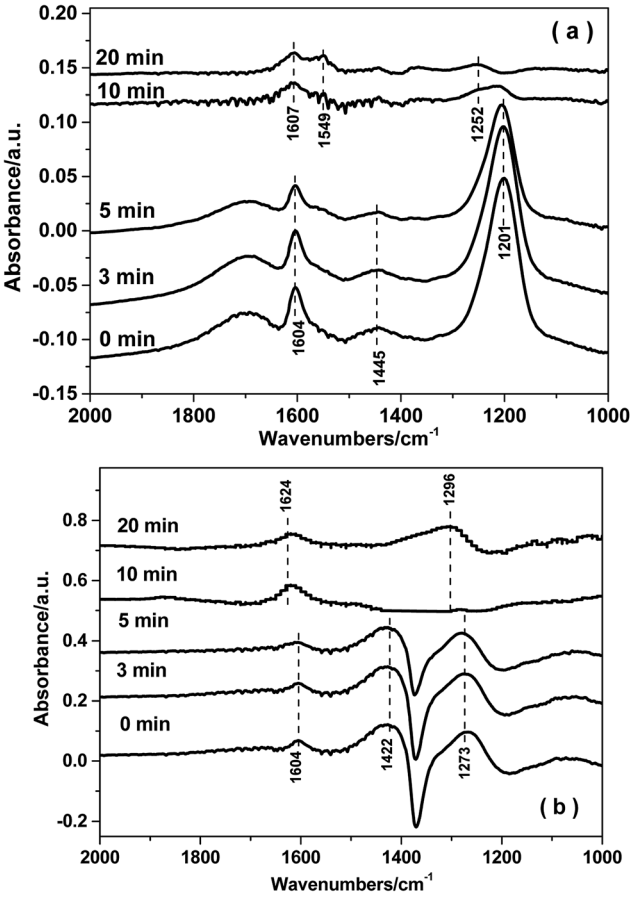

Fig. 11 *In situ* DRIFTS over $FeTiO_x$ (a) and $Fe_{0.9}Cu_{0.1}TiO_x$ (b) as a function of time in a flow of NO + O_2 after the catalysts were pre-exposed to a flow of NH_3 for 60 min followed by N_2 purging for 30 min at 250 °C.

With the increasing of the temperature to 250 °C, all bands attributed to NO_x adspecies vanished instantly, indicating that the absorbed nitrate and nitrite species were decomposed. This result indicated that the adsorption of nitrate species was decomposed at high temperature, leading to more active sites being available for the adsorption and activation of NH_3. Thus a higher catalytic activity was obtained. It is noted that the intensity of NO_x adspecies was strong below 200 °C. The results indicated that NO_x adspecies were easily adsorbed at low temperature on the catalysts, which was beneficial to the NH_3-SCR process at low temperature *via* L–H mechanism.

3.8.3. Reaction between nitrogen oxides and ammonia adspecies. Fig. 11 shows the *in situ* DRIFT spectra of the $FeTiO_x$ and $Fe_{0.9}Cu_{0.1}TiO_x$ catalysts as a function of time in a flow of NO + O_2 after the catalysts were pre-exposed to a flow of NH_3. The coordinated NH_3 on Lewis and Brønsted acid sites was formed on the catalysts with feeding NH_3. All bands due to ammonia adspecies diminished in 10 min after the catalysts were purged by NO + O_2, and subsequently NO_x adspecies were observed. NO_x readily reacted with surface-active NH_3 species over the $Fe_\alpha Cu_{1-\alpha}TiO_x$ catalyst. It could be concluded that the adsorbed NH_3 on the $Fe_\alpha Cu_{1-\alpha}TiO_x$ catalyst would react with gas-phase NO (Eley–Rideal mechanism) to form N_2 at 250 °C.

4. Conclusions

A series of $Fe_\alpha Cu_{1-\alpha}TiO_x$ catalysts with variable Cu doping amounts was directly synthesized by the sol–gel method, and their catalytic performances were tested for the selective catalytic reduction of NO with ammonia. The partial substitution of Fe by Cu could significantly promote the SCR activity of iron titanate catalysts, especially in the low temperature range. The highest activity was achieved on $Fe_{0.9}Cu_{0.1}Ti$ catalyst. NO conversion was above 80% and N_2 selectivity exceeded 90% on this catalyst in the temperature range of 200–375 °C. However, the N_2 selectivity showed an obvious decrease with the increasing of Cu substitution amounts, and there should be a compromise between the SCR activity and N_2 selectivity when we determine the Cu substitution amount in practical industrial applications.

High NO and NH_3 oxidation activities facilitated the high NH_3-SCR activities of the catalysts in the low-temperature range, while too strong NH_3 oxidation ability resulted in the decline of NH_3-SCR activity. DFT calculations show that the barrier of NH_3 activation is dramatically reduced with the doping of both Cu and Fe owing to the lowered p-band of lattice O. However, such

activated O will also strongly decrease the barrier for the dissociation of NH_2 to NH species, which will lead to the formation of N_2O and, accordingly, the decrease of N_2 selectivity.

The reaction mechanism for NH_3-SCR over the $Fe_{0.9}Cu_{0.1}$-TiO_x catalyst was studied by means of *in situ* DRIFT spectroscopy. The results demonstrated that both Brønsted and Lewis acid sites over $Fe_{0.9}Cu_{0.1}Ti$ catalyst were active in the NH_3-SCR reaction. On the one hand, NO_x adspecies were easily adsorbed at low temperature on the $Fe_{0.9}Cu_{0.1}TiO_x$ catalyst, which were beneficial to the NH_3-SCR process at low temperature *via* the L–H mechanism. On the other hand, the adsorption of nitrate species was decomposed at high temperature, leading to more active sites available for the adsorption and activation of NH_3. Thus a higher catalytic activity was obtained.

Conflicts of interest

There are no conflicts to declare.

Acknowledgements

This work was financially supported by the National Natural Science Foundation of China (21376261, 21173270, 21503273), 863 Program (2015AA034603), Scientific Research Foundation of China University of Petroleum Beijing (2462015YJRC005).

References

1 R. M. Heck, *Catal. Today*, 1999, **53**, 519–523.
2 V. Parvulescu, P. Grange and B. Delmon, *Catal. Today*, 1998, **46**, 233–316.
3 A. Fritz and V. Pitchon, *Appl. Catal., B*, 1997, **13**, 1–25.
4 Z. Ren, Y. Teng, L. Zhao and R. Wang, *Catal. Today*, 2017, **297**, 36–45.
5 J. Liu, J. Meeprasert, S. Namuangruk, K. Zha, H. Li, L. Huang, P. Maitarad, L. Shi and D. Zhang, *J. Phys. Chem. C*, 2017, **121**, 4970–4979.
6 Z. Fan, J. W. Shi, C. Gao, G. Gao, B. Wang and C. Niu, *ACS Appl. Mater. Interfaces*, 2017, **9**, 16117–16127.
7 F. Liu, H. He and C. Zhang, *Chem. Commun.*, 2008, **17**, 2043–2045.
8 F. Liu, H. He, C. Zhang, Z. Feng, L. Zhao, Y. Xie and T. Hu, *Appl. Catal., B*, 2010, **96**, 408–420.
9 F. Liu, K. Asakura, H. He, Y. Liu, W. Shan, X. Shi and C. Zhang, *Catal. Today*, 2011, **164**, 520–527.
10 F. Liu, K. Asakura, P. Xie, J. Wang and H. He, *Catal. Today*, 2013, **201**, 131–138.
11 F. Nakajima and I. Hamada, *Catal. Today*, 1996, **29**, 109–115.
12 X. Li, G. Lu, Z. Qu, D. Zhang and S. Liu, *Appl. Catal., A*, 2011, **398**, 82–87.
13 S. Roy, B. Viswanath, M. S. Hegde and G. Madres, *J. Phys. Chem. C*, 2008, **398**, 6002–6012.
14 D. Pietrogiacomi, A. Magliano, D. Sannino, M. C. Campa, P. Ciambelli and V. Indovina, *Appl. Catal., B*, 2005, **60**, 83–92.
15 T. Boningari, R. Koirala and P. G. Smirniotis, *Appl. Catal., B*, 2014, **127**, 255–264.
16 C. Sun, Z. Jie, Y. Lv, L. Qi, B. Liu, F. Gao, K. Sun, L. Dong and Y. Chen, *Appl. Catal., B*, 2011, **103**, 206–220.
17 G. Kresse and J. Furthmüller, *Phys. Rev. B: Condens. Matter Mater. Phys.*, 1996, **54**, 11169–11186.
18 G. Kresse and J. Furthmüller, *Comput. Mater. Sci.*, 1996, **6**, 15–50.
19 J. Perdew, K. Burke and M. Ernzerhof, *Phys. Rev. Lett.*, 1996, **77**, 3865–3868.
20 S. L. Dudarev, S. Y. Savrasov, C. J. Humphreys and A. P. Sutton, *Phys. Rev. B: Condens. Matter Mater. Phys.*, 1998, **57**, 1505–1509.
21 P. E. Blöchl, *Phys. Rev. B: Condens. Matter Mater. Phys.*, 1994, **50**, 17953–17979.
22 G. Henkelman, B. P. Uberuaga and H. Jónsson, *J. Chem. Phys.*, 2000, **113**, 9901.
23 G. Henkelman and H. Jónsson, *J. Chem. Phys.*, 2000, **113**, 9978.
24 W. Song, J. Liu, H. Zheng, S. Ma, Y. Wei, A. Duan, G. Jiang, Z. Zhao and E. J. Hensen, *Catal. Sci. Technol.*, 2016, **6**, 2120–2128.
25 X. Yao, L. Zhang, L. Li, L. Liu, Y. Cao, X. Dong, F. Gao, Y. Deng, C. Tang and Z. Chen, *Appl. Catal., B*, 2014, **150**, 315–329.
26 Y. Li, J. Deng, W. Song, J. Liu, Z. Zhao, M. Gao, Y. Wei and L. Zhao, *J. Phys. Chem. C*, 2016, **120**, 14669–14680.
27 G. Qi and R. T. Yang, *Appl. Catal., B*, 2003, **44**, 217–225.
28 G. Madia, M. Koebel, A. Martin Elsener and A. Wolkaun, *Ind. Eng. Chem. Res.*, 2002, **15**, 3512–3517.
29 R. Q. Long and R. T. Yang, *J. Catal.*, 2001, **198**, 20–28.
30 G. Lu, X. Li, Z. Qu, Q. Zhao, L. Zhao and G. Chen, *Chem. Eng. J.*, 2011, **168**, 1128–1133.
31 T. Zhang, J. Liu, D. Wang, Z. Zhao, Y. Wei, K. Cheng, G. Jiang and A. Duan, *Appl. Catal., B*, 2014, **148–149**, 520–531.
32 P. G. Smirniotis, D. A. Pena and B. S. Uphade, *Angew. Chem., Int. Ed.*, 2001, **40**, 2479–2482.
33 L. Lietti, I. Nova, G. Ramis, L. DallAcqua, G. Busca, E. Giamello, P. Forzatti and F. Bregani, *J. Catal.*, 1999, **187**, 419–435.
34 S. Guerrero, I. Guzmán, G. Aguila and A. Paulo, *Catal. Commun.*, 2009, **11**, 38–42.
35 M. Kantcheva, *Appl. Catal., B*, 2003, **42**, 89–109.